Predicting the charge density response in metal electrodes

Andrea Grisafi, Augustin Bussy, Mathieu Salanne, Rodolphe Vuilleumier

Predicting the charge density response in metal electrodes

Andrea Grisafi,[1,*] Augustin Bussy,[2] Mathieu Salanne,[3,4] and Rodolphe Vuilleumier[1]
[1]PASTEUR, Département de chimie, École Normale Supérieure, PSL University, Sorbonne Université, CNRS, 75005 Paris, France
[2]Department of Chemistry, University of Zurich, Winterthurerstrasse 190, 8057 Zürich, Switzerland
[3]Sorbonne Université, CNRS, Physicochimie des Électrolytes et Nanosystèmes Interfaciaux, 75005 Paris, France
[4]Institut Universitaire de France, 75231 Paris, France

(Received 17 April 2023; revised 18 August 2023; accepted 6 December 2023; published 22 December 2023)

The computational study of energy storage and conversion processes calls for simulation techniques that can reproduce the electronic response of metal electrodes under electric fields. Despite recent advancements in machine-learning methods applied to electronic-structure properties, predicting the nonlocal behavior of the charge density in electronic conductors remains a major open challenge. We combine long-range and equivariant kernel methods to predict the Kohn-Sham electron density of metal electrodes in response to various kinds of electric field perturbations. By taking slabs of gold as an example, we first show how the nonlocal electronic polarization generated by the interaction with an ionic species can be accurately reproduced in electrodes of arbitrary thickness. A finite-field extension of the method is then derived, which allows us to predict the charge transfer and the electrostatic potential drop induced by the application of a homogeneous and constant electric field. Finally, we demonstrate the capability of the method to reproduce the charge density response in a gold/electrolyte capacitor under an applied voltage, predicting the system polarization with a greater accuracy than state-of-the-art classical atomic-charge models.

DOI: 10.1103/PhysRevMaterials.7.125403

I. INTRODUCTION

The behavior of the electronic charge density in metal surfaces plays a decisive role in the study of energy storage and conversion processes occurring in batteries, capacitors, and electrocatalytic frameworks [1–3]. Its accurate computer simulation ultimately requires the adoption of first-principles methods that are capable of predicting the nonlocal response of an electronic conductor subject to an external perturbation. Density functional theory (DFT), in particular, has been widely applied to the description of metal interfaces in various research areas of surface chemistry and catalysis [4–6]. Depending on the specific application, different methods can be adopted to keep the metal at a constant charge [7,8] and fixed applied potential [9–14], as well as to induce a macroscopic polarization in the system due to the presence of an applied field [15–17]. In spite of the success of these approaches, the extensive use of DFT for the study of realistic metal interfaces is hindered by an unfavorable scaling with the system size, effectively limiting their applicability to a few hundred atoms [18,19].

Beyond first-principles approaches, classical molecular dynamics (MD) methods have also attracted major attention in the context of enabling the simulation of metal interfaces at the nanometric scale [20]. These methods go from the adoption of fluctuating atomic charges [21–25] to the use of image-charge boundary conditions [26,27]. The downside of MD is, of course, the lack of an explicit quantum treatment, which limits the description of the electrode either to a perfect metal approximation or to the adoption of a finite screening length computed from semiclassical Thomas-Fermi models [28,29]. For these reasons, reaching the level of accuracy of DFT in the large-scale simulation of the metal charge density represents a goal of paramount importance [30,31].

In recent years, many efforts have been devoted to the development of machine-learning (ML) methods dedicated to the prediction of the electronic charge density [32–41]. The success of these methods is mostly grounded in the interplay between a local decomposition of the scalar field and the adoption of local representations of the atomic structure that are used as input vectors of the ML model. When it comes to conducting systems, however, local ML models are expected to show strong limitations in predicting the variations of the charge density over large distances, especially in the presence of external fields. In fact, while some ML methods that explicitly incorporate long-range effects have already been developed [42–45], the study of charge transfer phenomena in electronic conductors has, to date, been limited to simplified charge-equilibration schemes that represent the electron density via a set of atomic charges [46–48]. Moreover, an explicit ML treatment of the charge density in metal surfaces under electric fields has thus far been investigated only by virtue of suitable response functions that enter conceptual DFT approaches [49,50].

In this article, we show how to combine long-range and equivariant learning methods to predict the nonlocal behavior of the charge density response in metal electrodes, sidestepping the need to rely on any self-consistent optimization procedure. After presenting the general theory (Sec. II), a paradigmatic example is discussed in which a classical Gaussian charge polarizes Au(100) slabs of increasing thickness

*andrea.grisafi@ens.psl.eu

(Sec. III). Then, a finite-field model suitable to treat the application of external electric fields is derived (Sec. IV) which can be used to accurately predict the charge transfer along the nonconducting direction. Finally, applications of the method are presented for the charge density response in a gold/electrolyte capacitor under an applied potential difference, which is validated on the system polarization vector and then used to predict the electrical double-layer contribution to the differential capacitance of the interface (Sec. V).

II. GENERAL THEORY

Let us start by considering the linear expansion of the electron density on an atom-centered basis $\chi_{n\lambda\mu}$ given by the product of radial Gaussian-type functions R_n^λ and spherical harmonics $Y_{\lambda\mu}$:

$$n_e(\boldsymbol{r}) \approx \sum_{in\lambda\mu} c_i^{n\lambda\mu} \sum_{ix,iy} \chi_{n\lambda\mu}(\boldsymbol{r} - \boldsymbol{r}_i - \boldsymbol{u}_{ix,iy}), \tag{1}$$

where $\boldsymbol{r}_i$ are the atomic positions in the unit cell and $\boldsymbol{u}_{ix,iy}$ are the cell translation vectors used to account for the two-dimensional periodicity of the metallic surface. We assume that the coefficients $c_i^{n\lambda\mu}$ come from a density-fitting procedure of a reference Kohn-Sham density.

The decomposition of Eq. (1) can be used within equivariant ML models to predict n_e in a highly transferable (atom-centered) fashion [35,41]. In this work, we rely on a recently optimized kernel-based method introduced in Ref. [40] known as symmetry-adapted learning of three-dimensional electron densities (SALTED). Within SALTED, a linear approximation of the density expansion coefficients is provided which satisfies the rotational symmetry of spherical harmonics, i.e., $\boldsymbol{c}_i^{n\lambda} = \sum_M \boldsymbol{k}_{iM}^\lambda \boldsymbol{b}_M^{n\lambda}$. Here, $\boldsymbol{b}_M^{n\lambda}$ are vector-valued regression weights of dimension $(2\lambda+1)$, and $\boldsymbol{k}_{iM}^\lambda$ is a symmetry-adapted kernel matrix of dimension $(2\lambda+1)^{\otimes 2}$ which encodes the similarity between the local structural features of atom i and those of a sparse selection of atoms $\{M\}$ belonging to the training set [51]. The complexity of the learning problem then comes down to the adoption of physically inspired structural representations of the atomic environment $\boldsymbol{P}_i^\lambda$ [52], which define the kernel matrix as an inner product over a suitable feature space [53], i.e., $\boldsymbol{k}_{iM}^\lambda = \boldsymbol{P}_i^\lambda \boldsymbol{P}_M^{\lambda\dagger}$.

A typical choice for $\boldsymbol{P}_i^\lambda$ consists of an equivariant generalization of the popular smooth overlap of atomic positions (SOAP) method [51,54]. This approach ultimately derives from the definition of a smooth Gaussian density distribution describing the local environment of atom i, i.e., $\rho_i(\boldsymbol{r}) = f_{\rm cut}(r) \sum_j e^{-\alpha|\boldsymbol{r}-\boldsymbol{r}_{ij}|^2}$, with j running over the atomic neighbors and $f_{\rm cut}(r)$ being a spherical cutoff function of radius $r_{\rm cut}$. By construction, the model thus neglects any long-range effect that occurs beyond $r_{\rm cut}$ in exchange for a high level of transferability. While this is generally not a problem [39,55], we aim to demonstrate that endowing the structural features with a long-range character is essential when dealing with metal surfaces. For this reason, we rely on a definition of $\boldsymbol{P}_i^\lambda$ based on long-distance equivariant (LODE) representations [42]. In particular, we adopt an implementation of LODE that combines information about the local atomic density $\rho_i(\boldsymbol{r})$ and a Hartree-like potential originated by the Gaussian density of the atoms of the entire system [56,57]:

$$V_i(\boldsymbol{r}) = f_{\rm cut}(r) \int d\boldsymbol{r}' \frac{\sum_j e^{-\alpha|\boldsymbol{r}'-\boldsymbol{r}_{ij}|^2}}{|\boldsymbol{r}'-\boldsymbol{r}|}. \tag{2}$$

Note that the cutoff function is here applied *after* the Coulomb operator, thus guaranteeing the inclusion of long-range information within the local environment of i. The descriptor of order λ is finally obtained from a symmetry-adapted tensor product of ρ_i and V_i expanded on a set of orthogonal radial and angular functions [56,58]:

$$P_i^{\lambda\mu}(nn'll') = \sum_{mm'} \rho_i^{nlm} V_i^{n'l'm'} \langle lm, l'm'|\lambda\mu\rangle, \tag{3}$$

where n and lm are the radial and angular indexes, respectively, and $\langle lm, l'm'|\lambda\mu\rangle$ are the Clebsch-Gordan coefficients used for the composition of angular momenta.

III. PREDICTION OF NONLOCAL POLARIZATION EFFECTS

We start by considering slabs of gold aligned perpendicular to the z axis which interact with a sodium cation Na^+ placed 4 Å from the upper metal surface. In particular, we consider symmetric Au(100) slabs made of two unit cell repetitions along the xy plane and spanning from 3 to 15 gold layers along z. A total of 240 training configurations are then generated by taking uniform random displacements of the atomic positions up to 2.5% of the lattice constant along the three Cartesian directions. The electrode polarization is simulated at the quantum mechanics/molecular mechanics (QM/MM) level of theory by representing the ion as a classical Gaussian charge [59]. Reference density coefficients $c_i^{n\lambda\mu}$ for the gold electrodes are obtained by performing calculations of n_e at the DFT/Perdew-Burke-Ernzerhof level [60], in combination with a density-fitting approach based on an overlap metric [61–63]. The learning target is finally defined as the difference between the perturbed electron densities and the electron densities of the corresponding isolated electrodes, i.e., $\Delta n_e = n_e - n_e^0$.

From a ML point of view, the ion-induced polarization of the metal electrode is expected to be naturally captured by a multispecies treatment of Eq. (3). This accounts for computing as many ρ_i and V_i as the number of chemical species a in the system [56,64], while letting i run exclusively on the gold atoms. With this procedure, we train SALTED/LODE models using a local cutoff of $r_{\rm cut} = 8$ Å, where the atom density and potential fields are defined from Gaussian widths of $\sigma = 0.5$ Å and $\sigma = 4.0$ Å, respectively. For comparison, SALTED/SOAP models are similarly trained by substituting V_i with ρ_i in Eq. (3). Further details about the reference calculations and machine-learning parameters are reported in the Supplemental Material (SM) [65] (see also Refs. [66–73] therein).

We put the method to the test on rigid gold electrodes that include from $n_{\rm L} = 19$ to $n_{\rm L} = 27$ atomic layers. In so doing, we extrapolate the charge density response over a range of distances between the two metal surfaces that extends well beyond that spanned by the training set. As an accuracy measure of the ion-induced charge transfer, we compute the metal

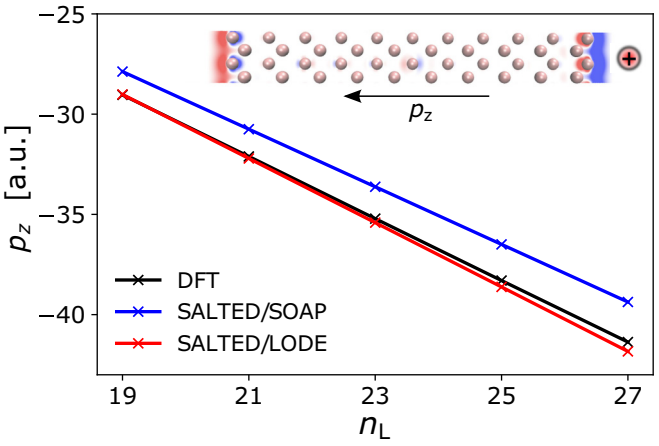

FIG. 1. Extrapolated electronic polarization p_z of Au(100) electrodes of increasing thickness n_L, induced by a Na^+ cation placed at 4 Å distance from the upper metal surface. Predictions are obtained for SALTED/SOAP (blue line) and SALTED/LODE (red line) models trained on the electron density response of electrodes that include up to $n_L = 15$ atomic layers. Black line: reference DFT polarization. Inset: volume slice of the predicted charge density response for an $n_L = 21$ gold electrode; the color code from blue to red corresponds to a linear scale from −0.001 to +0.001 a.u., respectively.

electronic polarization along z, which can be readily computed from the (0,0) and (1,0) spherical harmonics components of Δn_e:

$$\begin{aligned} p_z &= -\int_\Omega d\boldsymbol{r}\, z\, \Delta n_e(\boldsymbol{r}) \\ &= -\sum_{in} c_i^{n00}\, z_i\, \sqrt{4\pi} \int_0^\infty dr\, r^2 R_n^0(r) \\ &\quad -\sum_{in} c_i^{n10} \sqrt{\frac{4\pi}{3}} \int_0^\infty dr\, r^3 R_n^1(r), \end{aligned} \tag{4}$$

where the radial integrals are analytical when the basis functions are chosen to be Gaussian-type orbitals.

Figure 1 reports the prediction results as a function of the number of atomic layers n_L. As expected, we find that a local SOAP-based model is unable to reproduce the long-range character of the charge density response, resulting in predicted polarization values that are off by ∼36% of the standard deviation of p_z in the test set. Conversely, SALTED/LODE predictions are found to accurately extrapolate the electronic polarization at increasing electrode thicknesses, thus capturing the expected linear decrease of p_z with respect to n_L. This is confirmed by the density-derived calculation of the Hartree potential drop through the metallic slab, which is found to be in very good agreement with that of DFT for all the test electrodes considered [65]. We note that performing these predictions took ∼1 s per structure on a single node with 24 CPUs, resulting in a speedup of the order of 3×10^3 with respect to DFT [65].

A. Charge conservation

A crucial aspect of the method for the calculation of the derived electrostatic properties consists of guaranteeing that the predicted electron density response Δn_e integrates to zero. In this work, this condition is enforced exactly by *a posteriori* subtraction of the excess electronic charge Δq_e from the isotropic (0,0) density coefficients associated with the most diffuse radial functions $R^0_{n_{\max}}$:

$$\tilde{c}_i^{n_{\max}00} = c_i^{n_{\max}00} - \frac{1}{N_{\rm at}} \frac{\Delta q_e}{\sqrt{4\pi} \int_0^\infty dr\, r^2\, R^0_{n_{\max}}(r)}, \tag{5}$$

with the excess electronic charge given by

$$\Delta q_e = \int_\Omega d\boldsymbol{r}\, \Delta n_e^{\rm ML}(\boldsymbol{r}) = \sqrt{4\pi} \sum_{in} c_i^{n00} \int_0^\infty dr\, r^2\, R_n^0(r). \tag{6}$$

For SALTED/LODE models, we observe small absolute charge conservation errors $|\Delta q_e| < 0.01e$. Conversely, SALTED/SOAP predictions are associated with large errors $|\Delta q_e| > 0.1e$, highlighting the inadequacy of a local model to extrapolate the long-range response of the system; we refer to the SM [65] for further details.

IV. FINITE-FIELD RESPONSE

Having shown the importance of long-range structural information in describing the response properties of metal electrodes, we now proceed with investigating the charge transfer effect induced by an applied electric field. From here on, we will refer to only SALTED/LODE models. The accumulation or depletion of electronic charge at the two metal surfaces is simulated by performing calculations under a constant and uniform electric field along z. The field intensity is chosen to be $E_z = -1.0$ V/Å, which, for a perfect metal, corresponds to an induced surface charge of $\sigma = \pm 5.53 \times 10^{-3}\, e/\text{Å}^2$. DFT densities are generated from the same gold configurations and using the same level of theory already adopted in the previous example.

A. Derivation of finite-field representations

In order to reproduce the polarization of the electrode induced by an applied electric field E_z, the axial symmetry of the system around z must be explicitly incorporated into the ML model. To tackle this problem, we start by defining a potential-like descriptor that mimics the physical external perturbation in the local environment of the atoms. In particular, we consider the external potential $-E_z z$ centered at the position of a given atom i to enforce translational invariance, which is then cut off to limit the amount of information retained:

$$V_i^E(\boldsymbol{r}) = -E_z\, (z - z_i) f_{\rm cut}(r). \tag{7}$$

An equivariant descriptor $\boldsymbol{P}_i^{\lambda,E}$ that automatically satisfies the symmetry of the applied field can then be directly obtained by substituting V_i with V_i^E in Eq. (3). Given that the external potential has the same symmetry of (1,0) spherical harmonics, we obtain

$$\begin{aligned} P_i^{\lambda\mu,E} &= \sum_{mm'} \rho_i^{nlm}\, V_i^{n'l'm',E}\, \langle lm, l'm'|\lambda\mu\rangle \\ &= \sqrt{\frac{4\pi}{3}} E_z \left(\int_0^\infty dr\, r^3 R_{n'}(r) \right) \sum_m \rho_i^{anlm} \langle lm; 10|\lambda\mu\rangle. \end{aligned} \tag{8}$$

Note that from the rules of angular momentum composition we have $\mu = m + 0$ and $|l - 1| \leqslant \lambda \leqslant (l + 1)$ in the previous equation. Thus, the possible values for l are restricted to $(\lambda + 1, \lambda, |\lambda - 1|)$, while $m = \mu$. Moreover, enforcing the covariance under inversion operations implies $l + 1 + \lambda$ must be even, so that only the values for which $l = |\lambda \pm 1|$ survive. Interestingly, this result has a striking resemblance to the selection rules that are typically found in light-driven quantum transitions.

From Eq. (8), a ML representation of n_e able to reproduce the finite-field response, while not disregarding the nonlocal nature of the charge transfer, can finally be constructed as follows:

$$\tilde{\boldsymbol{P}}_i^{\lambda,E} \equiv \left(\boldsymbol{P}_i^{\lambda} \oplus \boldsymbol{P}_i^{\lambda,E}\right) \otimes \boldsymbol{P}_i^{0}, \tag{9}$$

with $\boldsymbol{P}_i^{\lambda}$ being the equivariant LODE representation of Eq. (3). Note that to preserve the desired symmetry properties, the tensor product with the field-independent LODE descriptor $\boldsymbol{P}_i^0$ is used to make the model nonlinear. Crucially, this operation allows us to introduce an effective coupling between the long-range structural features and the external field information. In practice, it is convenient to recast the algebraic operations reported in Eq. (9) in simple sums and products of the individual kernels, thus keeping the dimensionality of the learning problem unchanged with respect to the no-field case (kernel trick [74]):

$$\tilde{\boldsymbol{k}}_{ij}^{\lambda,E} = \left(\boldsymbol{k}_{ij}^{\lambda} + \boldsymbol{k}_{ij}^{\lambda,E}\right) \times k_{ij}^{0}. \tag{10}$$

B. Finite-field predictions

To test the capability of the previously discussed model to predict the electronic charge transfer induced by the applied electric field, we now repeat the size extrapolation exercise already carried out in the previous example, so the same training and test gold structures are used. Figure 2 reports the predicted charge density response for the largest test electrode considered, compared with the corresponding DFT profile. In spite of the highly extrapolative regime, our finite-field extension of LODE allows us to accurately reproduce the accumulation or depletion of opposite electronic charges on the two sides of the metal electrode, predicting a charge transfer of $0.2e$ that is in perfect agreement with that of DFT. To corroborate these results, we report in Fig. 2 the variation of the Hartree potential $\Delta\phi_{\mathrm{H}}$, which can be directly computed from the predicted Δn_e [65]. We find that the expected potential drop of $\sim$2 a.u. between the two metal surfaces is accurately predicted, reproducing the linear decrease of $\Delta\phi_{\mathrm{H}}$ in the metallic bulk in order to perfectly screen the opposite increase of the external potential $\phi_{\mathrm{ext}} = -E_z z$.

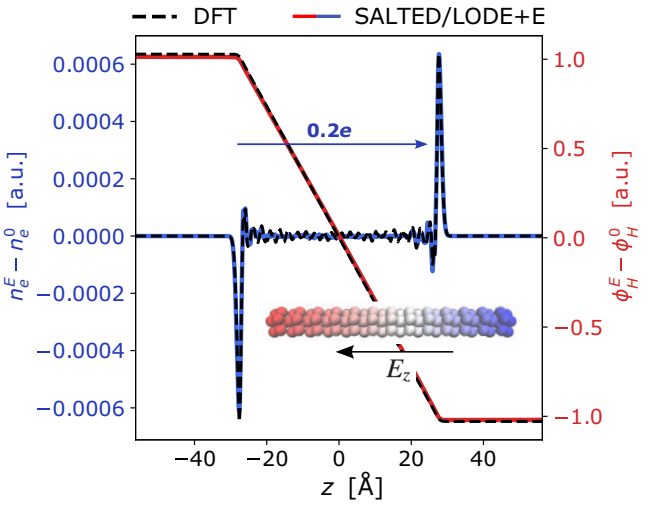

FIG. 2. Extrapolated density and potential response averaged over the xy plane of a Au(100) electrode with 27 metal layers under an applied electric field $E_z = -1$ V/Å. Blue line: electron density response. Red line: Hartree potential response. Black dashed line: reference DFT response. Predictions are obtained from a field-dependent SALTED/LODE+E model trained on a dataset which includes electrodes with $n_{\mathrm{L}}^{\mathrm{max}} = 15$. Inset: representation of the predicted $\phi_{\mathrm{H}}^E - \phi_{\mathrm{H}}^0$ through the metal electrode; the color code from blue to red corresponds to a linear scale from -1.0 to $+1.0$ a.u., respectively.

V. ELECTRODE POLARIZATION IN A GOLD/ELECTROLYTE IONIC CAPACITOR

We continue by showcasing an example in which a rigid Au(100) electrode made of four unit cell repetitions along the xy plane and seven metal layers is put in contact with a concentrated water/NaCl solution under a uniform electric field E_z [see Fig. 4(a) below]. Following Ref. [75], a similar setup can be used with three-dimensional periodic boundary conditions to simulate an ionic capacitor under an applied voltage $\Delta V = -E_z L_z$, with L_z being the length of the simulation box. In this example, an electric field $E_z = 0.016$ V/Å is applied to represent an ionic capacitor subject to a potential difference of $\Delta V = -1.0$ V. To generate electrolyte configurations that are representative of the given ensemble at $T = 298$ K, we run finite-E classical molecular dynamics [76]

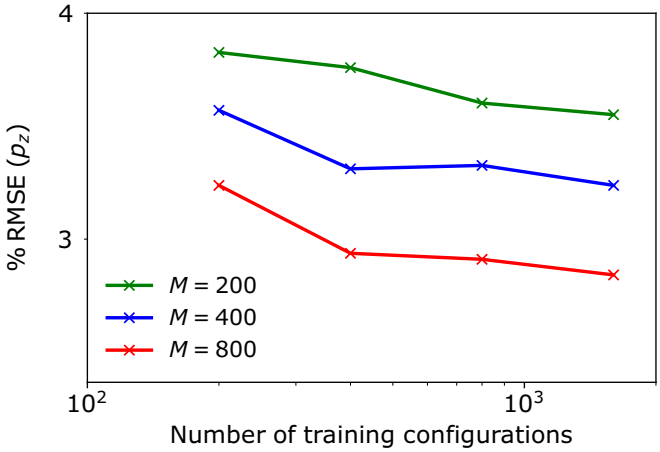

FIG. 3. Percent root-mean-square error (RMSE) of the electrode polarization p_z as predicted from SALTED/LODE models of the charge density response over a test set of 400 electrolyte configurations, reported as a function of the number of training configurations. Learning curves of different colors refer to different numbers of sparse atomic environments M used to reduce the dimensionality of the SALTED problem.

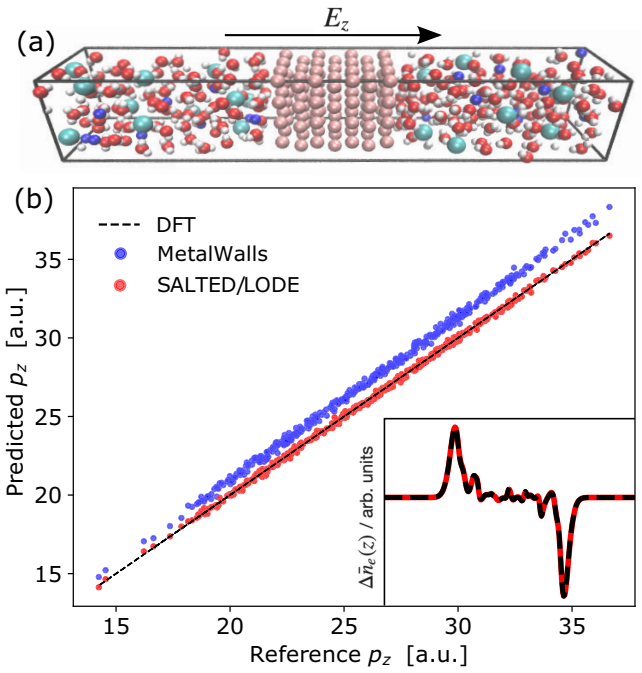

FIG. 4. (a) Representation of the physical system under study: a gold electrode is put in contact with a water/NaCl solution under an applied electric field $E_z = 0.016$ V/Å, corresponding to a potential drop of -1.0 V through the simulation cell [75]. (b) Electrode polarization p_z as predicted from the electron density response induced by 400 electrolyte configurations. Predictions are reported against the reference QM/MM values. Black dashed line: DFT. Blue dots: classical METALWALLS result [77]. Red dots: SALTED/LODE results. Inset: predicted electron density response averaged over the xy plane for a representative electrode/electrolyte configuration (red line), compared with the reference DFT profile.

over 10 ns, using the METALWALLS simulation program [77]. From the trajectory so generated, QM/MM calculations of the electrode charge density under the applied electric field E_z are then performed for 2000 uncorrelated configurations. In particular, we treat the gold slab at the same DFT level of theory already adopted in the previous examples, while representing the aqueous electrolyte via classical Gaussian charges [59]. Note that because of the classical nature of the electrolyte, setting the electrode in the middle of the simulation box is enough to avoid problems related to the discontinuous jump of the external potential at $z = L_z$. The difference between the QM/MM density and the density of the isolated electrode under E_z is finally considered as a learning target of the SALTED problem.

A. Validation of the SALTED/LODE model

We select 1600 random configurations for training and retain the remaining 400 for testing. SALTED/LODE models are constructed from atom density and potential fields defined from Gaussian widths of $\sigma = 0.5$ Å and $\sigma = 1.0$ Å, respectively, which are both cut off at $r_{\text{cut}} = 10$ Å. In Fig. 3, we report learning curves associated with the density-derived prediction of the electronic polarization p_z of the Au(100) electrode for the 400 randomly selected validation structures by comparing them with results obtained with different numbers of sparse atomic environments M. Root-mean-square errors are measured as a fraction of the standard deviation of p_z in the test set. We observe that while the accuracy of the model increases with the number of training structures, increasing the value of M is determinant for lowering the errors of SALTED/LODE predictions below 3%.

Figure 4(b) reports the ML predictions of p_z against the reference DFT values for the most accurate regression task performed with $M = 800$ and $N = 1600$. In so doing, we also compare results obtained from the classical METALWALLS simulation. We observe that METALWALLS yields a systematic overestimation of the electrode polarization, which accounts for an average deviation of $\langle \Delta p_z \rangle = 1.2$ a.u. with respect to DFT. Conversely, our SALTED/LODE model is able to accurately reproduce the charge density response induced by the field of the various electrolyte configurations. This is in line with the excellent agreement between the DFT and predicted response averaged over the xy plane $\Delta\bar{n}(z)$ as reported in the inset of Fig. 4(b) for a representative test configuration. Performing similar predictions took, on average, ∼5 s per structure on 128 CPUs versus ∼5 min for DFT. A substantial speedup of the ML performance will be achieved in the future by relying on a particle mesh Ewald implementation of the LODE potential [78].

B. Calculation of the differential capacitance

We conclude by providing an estimate of the electrical double-layer (EDL) contribution to the differential capacitance of the system, defined from the electrolyte-induced fluctuations of the integrated charge $\pm Q$ accumulated at the two metal surfaces [25]:

$$C_{\text{diff}}^{\text{EDL}} = \beta \, \langle (Q - \langle Q \rangle)^2 \rangle. \tag{11}$$

Computing Q from the charge density response implies taking either the right or left integral Δn_e from the middle of the slab to the classical electrolyte region. This can be computed analytically from the isotropic (0,0) density coefficients of the atoms that belong to one of the two sides of the metallic slab. For instance, upon setting the central metal layer at $z = 0$, we can write

$$\begin{aligned} Q_{\text{right}} &= -\int_{z>0} d\boldsymbol{r} \Delta n_e(\boldsymbol{r}) \\ &= -\sqrt{4\pi} \sum_{i \in z>0} \sum_{n} c_i^{n00} \int_0^\infty dr \, r^2 \, R_n^0(r). \end{aligned} \tag{12}$$

Upon predicting Q for 5500 uncorrelated frames of a METALWALLS trajectory of 30 ns, we obtain $C_{\text{diff}}^{\text{EDL}} = 8.9\,\mu\text{F/cm}^2$. This value is sensibly smaller than what can be obtained from the classical METALWALLS simulation, i.e., $C_{\text{diff}}^{\text{EDL}} = 10.5\,\mu\text{F/cm}^2$, which is found to give larger fluctuations of the electrode surface charge with respect to the corresponding ML predictions [65]. By and large, these results highlight the importance of going beyond a classical picture when describing nonlocal polarization effects in finite conducting materials.

VI. CONCLUSIONS

The presented study shows how the interplay of equivariant, long-range and finite-field learning models can be used to accurately predict the electronic response of metal electrodes under electric fields of different natures. The ready access to the charge density response can provide a rigorous pathway to accurately compute the polarization energy of generic electrochemical interfaces, while accurately incorporating the permanent electrostatics via local ML models of the electron density [39]. Crucially, the nonlocal nature of the LODE atomistic representation allows us to directly learn and predict the self-consistent charge density response, thus bypassing the need to incorporate self-consistency at the machine-learning level. In fact, this aspect positions our method as an attractive alternative to charge-equilibration models [47,48] by also enabling access to the quantum-level details of the electronic distribution beyond isotropic atomic charges. In perspective, an application of major impact will consist of driving the long-range dynamics of the system at the ML/MM level of theory [30], thanks to the calculation of the electric field associated with the predicted charge density distribution. Finally, we foresee applications of the method to determine the capability of the metal surface to undergo electron-transfer processes [79], as well to predict optical response functions [80] that can serve as a spectroscopic characterization of the interface [81].

An open-source implementation of SALTED which includes the extension to finite electric fields is available from GitHub [82]. Training data and configurations, as well as inputs for performing the reference CP2K calculations, are free to download from Zenodo [83]. A modified version of the CP2K program able to print out reference density coefficients needed for training the ML model is also available from GitHub [84]. The METALWALLS simulation program used to generate the classical finite-field trajectories is available from GitLab [85].

ACKNOWLEDGMENTS

The authors are grateful to A. P. Seitsonen, F. Grasselli, and K. Rossi for useful discussions. A.G. acknowledges funding from the Swiss National Science Foundation, Grant No. P2ELP2_199747. This work was supported by the French National Research Agency under the France 2030 program (Grant No. ANR-22-PEBA-0002). Simulations of the ionic capacitor were performed on the Luxembourg national supercomputer MeluXina (Grant No. EHPC-REG-2022R02-244).

[1] A. K. Lautar, J. Bitenc, T. Rejec, R. Dominko, J.-S. Filhol, and M.-L. Doublet, J. Am. Chem. Soc. **142**, 5146 (2020).
[2] S. D. Beinlich, N. G. Hörmann, and K. Reuter, ACS Catal. **12**, 6143 (2022).
[3] N. Karmodak, L. Bursi, and O. Andreussi, J. Phys. Chem. Lett. **13**, 58 (2022).
[4] J. K. Nórskov, F. Abild-Pedersen, F. Studt, and T. Bligaard, Proc. Natl. Acad. Sci. USA **108**, 937 (2011).
[5] B. Grosjean, M.-L. Bocquet, and R. Vuilleumier, Nat. Commun. **10**, 1656 (2019).
[6] N. Gerrits, E. W. F. Smeets, S. Vuckovic, A. D. Powell, K. Doblhoff-Dier, and G.-J. Kroes, J. Phys. Chem. Lett. **11**, 10552 (2020).
[7] A. M. Souza, I. Rungger, C. D. Pemmaraju, U. Schwingenschloegl, and S. Sanvito, Phys. Rev. B **88**, 165112 (2013).
[8] C. Freysoldt, A. Mishra, M. Ashton, and J. Neugebauer, Phys. Rev. B **102**, 045403 (2020).
[9] A. Y. Lozovoi, A. Alavi, J. Kohanoff, and R. M. Lynden-Bell, J. Chem. Phys. **115**, 1661 (2001).
[10] J.-S. Filhol and M. Neurock, Angew. Chem., Int. Ed. **45**, 402 (2006).
[11] K. Letchworth-Weaver and T. A. Arias, Phys. Rev. B **86**, 075140 (2012).
[12] N. G. Hörmann, O. Andreussi, and N. Marzari, J. Chem. Phys. **150**, 041730 (2019).
[13] M. M. Melander, M. J. Kuisma, T. E. K. Christensen, and K. Honkala, J. Chem. Phys. **150**, 041706 (2019).
[14] F. Domínguez-Flores and M. M. Melander, J. Chem. Phys. **158**, 144701 (2023).
[15] M. Stengel and N. A. Spaldin, Phys. Rev. B **75**, 205121 (2007).
[16] F. Che, J. T. Gray, S. Ha, and J.-S. McEwen, ACS Catal. **7**, 551 (2017).
[17] C. Ke, Z. Lin, and S. Liu, ACS Catal. **12**, 13542 (2022).
[18] R. Khatib, A. Kumar, S. Sanvito, M. Sulpizi, and C. S. Cucinotta, Electrochim. Acta **391**, 138875 (2021).
[19] A. Chen, J.-B. Le, Y. Kuang, and J. Cheng, J. Chem. Phys. **157**, 094702 (2022).
[20] G. Jeanmairet, B. Rotenberg, and M. Salanne, Chem. Rev. **122**, 10860 (2022).
[21] J. I. Siepmann and M. Sprik, J. Chem. Phys. **102**, 511 (1995).
[22] S. K. Reed, O. J. Lanning, and P. A. Madden, J. Chem. Phys. **126**, 084704 (2007).
[23] S. K. Reed, P. A. Madden, and A. Papadopoulos, J. Chem. Phys. **128**, 124701 (2008).
[24] D. T. Limmer, C. Merlet, M. Salanne, D. Chandler, P. A. Madden, R. van Roij, and B. Rotenberg, Phys. Rev. Lett. **111**, 106102 (2013).
[25] L. Scalfi, D. T. Limmer, A. Coretti, S. Bonella, P. A. Madden, M. Salanne, and B. Rotenberg, Phys. Chem. Chem. Phys. **22**, 10480 (2020).
[26] M. K. Petersen, R. Kumar, H. S. White, and G. A. Voth, J. Phys. Chem. C **116**, 4903 (2012).
[27] K. A. Dwelle and A. P. Willard, J. Phys. Chem. C **123**, 24095 (2019).
[28] L. Scalfi, T. Dufils, K. G. Reeves, B. Rotenberg, and M. Salanne, J. Chem. Phys. **153**, 174704 (2020).
[29] L. Scalfi and B. Rotenberg, Proc. Natl. Acad. Sci. USA **118**, e2108769118 (2021).
[30] N. Di Pasquale, J. D. Elliott, P. Hadjidoukas, and P. Carbone, J. Chem. Theory Comput. **17**, 4477 (2021).

[31] N. Di Pasquale, A. R. Finney, J. D. Elliott, P. Carbone, and M. Salvalaglio, J. Chem. Phys. **158**, 134714 (2023).
[32] F. Brockherde, L. Vogt, L. Li, M. E. Tuckerman, K. Burke, and K. R. Müller, Nat. Commun. **8**, 872 (2017).
[33] J. M. Alred, K. V. Bets, Y. Xie, and B. I. Yakobson, Compos. Sci. Technol. **166**, 3 (2018).
[34] A. Chandrasekaran, D. Kamal, R. Batra, C. Kim, L. Chen, and R. Ramprasad, npj Comput. Mater. **5**, 22 (2019).
[35] A. Grisafi, A. Fabrizio, B. Meyer, D. M. Wilkins, C. Corminboeuf, and M. Ceriotti, ACS Cent. Sci. **5**, 57 (2019).
[36] A. Fabrizio, A. Grisafi, B. Meyer, M. Ceriotti, and C. Corminboeuf, Chem. Sci. **10**, 9424 (2019).
[37] M. Bogojeski, L. Vogt-Maranto, M. E. Tuckerman, K.-R. Müller, and K. Burke, Nat. Commun. **11**, 5223 (2020).
[38] P. B. Jørgensen and A. Bhowmik, npj Comput. Mater. **8**, 183 (2022).
[39] A. M. Lewis, A. Grisafi, M. Ceriotti, and M. Rossi, J. Chem. Theory Comput. **17**, 7203 (2021).
[40] A. Grisafi, A. M. Lewis, M. Rossi, and M. Ceriotti, J. Chem. Theory Comput. **19**, 4451 (2023).
[41] J. A. Rackers, L. Tecot, M. Geiger, and T. E. Smidt, Mach. Learn.: Sci. Technol. **4**, 015027 (2023).
[42] A. Grisafi and M. Ceriotti, J. Chem. Phys. **151**, 204105 (2019).
[43] A. Gao and R. C. Remsing, Nat. Commun. **13**, 1572 (2022).
[44] L. Zhang, H. Wang, M. C. Muniz, A. Z. Panagiotopoulos, R. Car, and W. E, J. Chem. Phys. **156**, 124107 (2022).
[45] J. Westermayr, S. Chaudhuri, A. Jeindl, O. T. Hofmann, and R. J. Maurer, Digital Discovery **1**, 463 (2022).
[46] S. A. Ghasemi, A. Hofstetter, S. Saha, and S. Goedecker, Phys. Rev. B **92**, 045131 (2015).
[47] T. W. Ko, J. A. Finkler, S. Goedecker, and J. Behler, Nat. Commun. **12**, 398 (2021).
[48] C. G. Staacke, S. Wengert, C. Kunkel, G. Csányi, K. Reuter, and J. T. Margraf, Mach. Learn.: Sci. Technol. **3**, 015032 (2022).
[49] Y. Shao, L. Andersson, L. Knijff, and C. Zhang, Electron. Struct. **4**, 014012 (2022).
[50] T. Dufils, L. Knijff, Y. Shao, and C. Zhang, J. Chem. Theory Comput. **19**, 5199 (2023).
[51] A. Grisafi, D. M. Wilkins, G. Csányi, and M. Ceriotti, Phys. Rev. Lett. **120**, 036002 (2018).
[52] F. Musil, A. Grisafi, A. P. Bartók, C. Ortner, G. Csányi, and M. Ceriotti, Chem. Rev. **121**, 9759 (2021).
[53] V. L. Deringer, A. P. Bartók, N. Bernstein, D. M. Wilkins, M. Ceriotti, and G. Csányi, Chem. Rev. **121**, 10073 (2021).
[54] A. P. Bartók, R. Kondor, and G. Csányi, Phys. Rev. B **87**, 184115 (2013).
[55] A. Fabrizio, K. Briling, A. Grisafi, and C. Corminboeuf, Chimia **74**, 232 (2020).
[56] A. Grisafi, J. Nigam, and M. Ceriotti, Chem. Sci. **12**, 2078 (2021).
[57] K. K. Huguenin-Dumittan, P. Loche, N. Haoran, and M. Ceriotti, J. Phys. Chem. Lett. **14**, 9612 (2023).
[58] M. J. Willatt, F. Musil, and M. Ceriotti, J. Chem. Phys. **150**, 154110 (2019).
[59] T. Laino, F. Mohamed, A. Laio, and M. Parrinello, J. Chem. Theory Comput. **2**, 1370 (2006).
[60] J. P. Perdew, K. Burke, and M. Ernzerhof, Phys. Rev. Lett. **77**, 3865 (1996).
[61] O. Vahtras, J. Almlöf, and M. Feyereisen, Chem. Phys. Lett. **213**, 514 (1993).
[62] K. R. Briling, A. Fabrizio, and C. Corminboeuf, J. Chem. Phys. **155**, 024107 (2021).
[63] A. Bussy, O. Schütt, and J. Hutter, J. Chem. Phys. **158**, 164109 (2023).
[64] M. J. Willatt, F. Musil, and M. Ceriotti, Phys. Chem. Chem. Phys. **20**, 29661 (2018).
[65] See Supplemental Material at http://link.aps.org/supplemental/10.1103/PhysRevMaterials.7.125403 for details of the dataset generation, a derivation of the finite-field extension of LODE, details of the ML parameters, a discussion of charge conservation, complementary results, an explicit calculation of the electronic polarization vector, and a discussion of the calculation of the differential capacitance.
[66] G. J. Martyna and M. E. Tuckerman, J. Chem. Phys. **110**, 2810 (1999).
[67] P. Minárу, M. E. Tuckerman, K. A. Pihakari, and G. J. Martyna, J. Chem. Phys. **116**, 5351 (2002).
[68] J. L. F. Abascal and C. Vega, J. Chem. Phys. **123**, 234505 (2005).
[69] G. Imbalzano, A. Anelli, D. Giofré, S. Klees, J. Behler, and M. Ceriotti, J. Chem. Phys. **148**, 241730 (2018).
[70] T. D. Kühne, M. Iannuzzi, M. Del Ben, V. V. Rybkin, P. Seewald, F. Stein, T. Laino, R. Z. Khaliullin, O. Schütt, F. Schiffmann, D. Golze, J. Wilhelm, S. Chulkov, M. H. Bani-Hashemian, V. Weber, U. Borštnik, M. Taillefumier, A. S. Jakobovits, A. Lazzaro, H. Pabst *et al.*, J. Chem. Phys. **152**, 194103 (2020).
[71] S. Nosé, J. Chem. Phys. **81**, 511 (1984).
[72] G. L. Stoychev, A. A. Auer, and F. Neese, J. Chem. Theory Comput. **13**, 554 (2017).
[73] S. Goedecker, M. Teter, and J. Hutter, Phys. Rev. B **54**, 1703 (1996).
[74] S. Theodoridis and K. Koutroumbas, *Pattern Recognition*, 4th ed. (Academic, Cambridge Massachusetts, 2009).
[75] T. Dufils, G. Jeanmairet, B. Rotenberg, M. Sprik, and M. Salanne, Phys. Rev. Lett. **123**, 195501 (2019).
[76] C. Zhang, T. Sayer, H. Hutter, and M. Sprik, J. Phys.: Energy **2**, 032005 (2020).
[77] A. Marin-Laflèche, M. Haefele, L. Scalfi, A. Coretti, T. Dufils, G. Jeanmairet, S. K. Reed, A. Serva, R. Berthin, C. Bacon, S. Bonella, B. Rotenberg, P. A. Madden, and M. Salanne, J. Open Source Software **5**, 2373 (2020).
[78] T. Darden, D. York, and L. Pedersen, J. Chem. Phys. **98**, 10089 (1993).
[79] A. K. Lautar, A. Hagopian, and J.-S. Filhol, Phys. Chem. Chem. Phys. **22**, 10569 (2020).
[80] A. M. Lewis, P. Lazzaroni, and M. Rossi, J. Chem. Phys. **159**, 014103 (2023).
[81] A. U. Chowdhury, N. Muralidharan, C. Daniel, R. Amin, and I. Belharouak, J. Power Sources **506**, 230173 (2021).
[82] https://github.com/andreagrisafi/SALTED.
[83] https://zenodo.org/records/10229714.
[84] https://github.com/abussy/cp2k/tree/ml_print.
[85] https://gitlab.com/ampere2/metalwalls.